metals

MDPI

Article

Electrochemical Determination of Ascorbic Acid by Mechanically Alloyed Super Duplex Stainless Steel Powders

Rayappa Shrinivas Mahale [1,2], Shamanth Vasanth [1,*], Sharath Peramenahalli Chikkegouda [3,4], Shashanka Rajendrachari [5,*], Damanapeta Narsimhachary [6] and Nagaraj Basavegowda [7,*]

1 School of Mechanical Engineering, REVA University, Bengaluru 560064, India; rayappamahale@gmail.com
2 Department of Mechanical Engineering, Jain College of Engineering and Research, Udyambag, Belagavi 590008, India
3 Department of Metallurgical and Materials Engineering, Faculty of Engineering and Technology, Jain Deemed to be University, Bengaluru 562112, India; pc.sharath@jainuniversity.ac.in
4 Department of Electronics and Communication, Faculty of Engineering and Technology, Jain Deemed to be University, Bengaluru 562112, India
5 Department of Metallurgical and Materials Engineering, BARTIN University, Bartin 74100, Turkey
6 Department of Mechanical Engineering, School of Engineering and Technology, G H Raisoni University, Saikheda, G H Raisoni Nagar, Gram Doda, Borgaon 480337, India; narsimhachary.damanapeta@ghru.edu.in
7 Department of Biotechnology, Yeungnam University, Gyeongsan 38541, Republic of Korea
* Correspondence: shamanth.v@reva.edu.in (S.V.); shashanka@bartin.edu.tr (S.R.); nagarajb@yu.ac.kr (N.B.)

Abstract: SAF-2507 super duplex stainless steel powders (SDSS) were prepared using a high-energy planetary ball milling process. The X-ray diffraction (XRD) shows peak broadening after 20 h of ball milling and revealed a phase transformation resulting in a two-phase alloy mixture containing nearly equal amounts of ferrite (α) and austenite (γ). After 20 h of ball milling the particle size was reduced to ~201 nm. Scanning electron microscope (SEM) micrographs showed small-size irregular grains with an average particle size ranging from 5–7 μm. The high-resolution transmission microscope (HRTEM) analysis confirmed the presence of nanocrystalline particles with sizes ranging from 10 to 50 nm. The presence of ferrite phase is visible in the corresponding diffraction pattern as well. In this paper, we have discussed the electrochemical sensor application of mechanically alloyed nano-structured duplex stainless steel powders. The fabricated 4 mg duplex stainless steel modified carbon paste electrode (SDSS-MCPE) has shown excellent current sensitivity in comparison with 2, 6, 8, and 10 mg SDSS-MCPEs during the detection of ascorbic acid (AA) in a phosphate buffer solution with a pH of 6.8. The calculated electrode active surface area of SDSS-MCPE was found to be almost two times larger than the surface area of the bare carbon paste electrode (BCPE). The limit of detection (LD) and limit of quantification (LQ) were found to be 0.206×10^{-8} M and 0.688×10^{-8} M, respectively, for the fabricated 4 mg SDSS-MCPE.

Keywords: super duplex stainless steel; mechanical alloying; cyclic voltammetry; modified carbon paste electrode; electro-oxidation

check for updates

Citation: Mahale, R.S.; Vasanth, S.; Chikkegouda, S.P.; Rajendrachari, S.; Narsimhachary, D.; Basavegowda, N. Electrochemical Determination of Ascorbic Acid by Mechanically Alloyed Super Duplex Stainless Steel Powders. *Metals* **2023**, *13*, 1430. https://doi.org/10.3390/met13081430

Academic Editors: Wei Liu, Henrik K. Hansen and Chang Woo Lee

Received: 22 May 2023
Revised: 24 July 2023
Accepted: 7 August 2023
Published: 9 August 2023

Copyright: © 2023 by the authors. Licensee MDPI, Basel, Switzerland. This article is an open access article distributed under the terms and conditions of the Creative Commons Attribution (CC BY) license (https://creativecommons.org/licenses/by/4.0/).

1. Introduction

Stainless steels are a sought-after choice for a variety of applications because of their remarkable corrosion resistance, formability, and aesthetically pleasing appearance. Nevertheless, due to their low heat conductivity, strong built-up edge (BUE) forming ability, and high deformation hardening, stainless steels are more challenging to process than other alloy steels [1]. In super duplex stainless steels (SDSS) ferrite and austenite are the sole phases. The structure's ferrite phase contributes to its increased strength, while the austenite phase ensures toughness and improved corrosion resistance [2–5]. Due to their superior toughness, weldability, excellent corrosion resistance, high energy absorption, and greater tensile strength in comparison to single-phase ferritic and austenitic stainless steel,

super duplex stainless steels are used in the nuclear power, petroleum, chemical, paper, pulp, and marine industries [6–14].

Due to its widespread application in various industries, steel has long been the subject of research. The structure and quality of steel have been improved via the use of several processing techniques. It is anticipated that the future advancement of steel will be possible through crystalline structural refinement to the nanoscale. In recent years, many techniques, such as hydrostatic extrusion, equivalent channel angular pressing, and high-pressure torsion, have been developed to improve the architecture of alloys and metals through significant plastic deformation [15,16].

Ball milling is one of the successful techniques for producing nanocrystalline alloys, which is proceeded by efficient powder compressing that maintains the nanocrystalline structure. Super duplex stainless steel with a nanocrystal condition was attempted to be obtained in this study using the planetary ball milling approach [17,18]. Ball milling is an efficient and user-friendly procedure that involves adding a predetermined amount of powder material into a mill vial and processing it through contact with balls (milling media) and friction between the balls and the walls of the vial [19].

The planetary ball mill is one of the most popular methods and is effective at the same time. Particle size reduction in a range of nanometers has been accomplished using this method. Ball milling has a substantial impact on mechanical deformation, surface modification, and particle and crystallite size reduction in powder samples. Chemical reactions that are infrequently triggered at room temperature can be induced using this technique. Ball milling is more often used in various material science investigations because of this, and more recently, in most of the research involving hydrogen storage materials [20–24]. It may be used in a variety of ways, including ball milling, mechanical alloying, and reactive ball milling. Since the material transfer happens through diffusion processes, planetary ball milling is employed to induce metastable phase transition by integrating nanoscale structure [25].

Shashanka and Chaira prepared powders of austenitic and ferritic stainless steel using a dual-drive planetary mill and a Fritsch Pulverisette planetary mill. The milling time for dual-drive planetary mills was 10 h, and the milling time for Fritsch Pulverisette planetary mills was 40 h. After 10 h of ball milling in a dual-drive planetary mill using toluene as a process control agent, they discovered that the crystallite size decreased from 9 nm for austenitic stainless steel and 11 nm for ferritic stainless steel, thereby increasing the lattice strain [26]. In the presence of a purified nitrogen gas atmosphere, Haghir et al., used a Fe-18Cr-11Mn powder combination as a starting material. The ball mill used was a Retsch PM-100. After 100 h of milling, the partial amorphization of the crystal structure was observed. According to the studies, increasing the milling time causes the austenite phase (γ) to be observed in the XRD patterns, and the nitrogen atmosphere aids in the complete phase transformation from ferrite (α) to austenite (γ) [27]. Amini et al., used Fe-18Cr-4Mn alloy combinations in a Fritsch planetary ball mill. The powders were ball milled in a nitrogen gas atmosphere. According to the findings, the milling atmosphere has a significant impact on phase transformation and amorphization. The nitrogen gas atmosphere promotes amorphization by infusing nitrogen atoms into the powder mixture. After 126 h of ball milling, the solid solution achieved complete amorphization [28]. This study includes SAF-2507, a premium alloy super duplex steel designed for use in extremely corrosive environments. It contains high levels of chromium, molybdenum, and nitrogen and was developed primarily for applications subjected to severe stress in salt environments (saltwater) [29–32].

SUDOSCAN, a very effective non-invasive method for the early detection of diabetes, was created by Ayoub et al. [33] using stainless steel 304L. The authors used stainless steel 304L as a nickel replacement material. This substance, which is also less expensive than nickel, is frequently utilized in surgical supplies. The study sought to investigate the stainless steel 304L's clinical uses for identifying different factors in sweat. For the electrogenerated chemiluminescence application (ECL), Kitte et al., employed stainless

steel electrodes [34]. ECL is a method whereby species produced at electrodes are engaged in electron transfer processes and enter excited states that release light as a result. For the ECL investigation, the authors employed stainless steel as the working electrode. Because stainless steel has excellent electrical conductivity and high mechanical strength, the authors discovered that using stainless steel electrodes considerably improves the sensitivity to detect glucose and H_2O_2. A 316-grade stainless steel was employed by Bimakr et al., for the electrochemical monitoring of biofilm development in chlorinated drinking water systems [35].

Chemically inert stainless steel is also affordable and corrosion resistant. According to the findings, stainless steel may be a more sensitive electrode material for identifying minute variations in cell density during the development of biofilms. Since 304-grade stainless steel has strong corrosion resistance, excellent biocompatibility, and is inexpensive, Faria et al., employed it for electrochemical biosensing applications [36]. Due to the presence of carriers for donors and acceptors that exhibit both n- and p-type behaviors, Mott–Schottky analysis showed that the corrosion products on the surface of 304 stainless steel exhibit semiconducting characteristics. A stainless steel voltammetric sensor was created by Martínez-Ibernón et al., to monitor changes in humidity and oxygen availability in reinforced concrete constructions [37]. Due to both its low cost in comparison to other metals and its resilience in a variety of hostile situations, the material is chosen for the sensor application. González et al., created electrodes for electrochemical sensing by immobilizing graphene-based nanocomposites on AISI 316L stainless steel substrates [38]. Stainless steels have intriguing properties that make them suitable for use in biomedical applications, including their great corrosion resistance, outstanding biocompatibility, and low cost. Additionally, stainless steels (SS) are interesting candidates to serve as the transducer substrate of devices for electrochemical sensing due to their excellent electrical conductivity and comparatively inexpensive cost. According to the tests, an alkaline medium with a linear range of 0.01 mM to 0.7 mM and a response time of less than 5 s might be used to detect glucose using an AISI 316L electrode.

Ascorbic acid exhibits intriguing electrochemical sensing behaviors due to its redox characteristics. Ascorbic acid can undergo oxidation and reduction reactions that can be used to detect it electrochemically. In an electrochemical sensing system, a working electrode is often utilized to facilitate analyte redox reactions. When it comes to ascorbic acid, the most commonly used electrochemical approach is cyclic voltammetry (CV). Cyclic voltammetry includes sweeping the applied potential through a range and measuring the resulting current. The resulting voltammogram offers useful information regarding the redox behavior of ascorbic acid.

Ascorbic acid can be oxidized to generate dehydroascorbic acid in an aqueous solution at a low potential. This oxidation process involves the loss of two electrons and two protons and is commonly detected at +0.1 to +0.2 V vs. a reference electrode. The electro-oxidation of ascorbic acid involves the transfer of electrons from ascorbic acid molecules to the electrode surface. Various factors, including the concentration of the stainless steel material, can influence this oxidation process. Higher concentrations of super duplex stainless steel may enhance the active surface area for electrochemical processes, boosting ascorbic acid electro-oxidation.

The use of super duplex stainless steel as an electrochemical sensor was investigated in the present study using cyclic voltammetric techniques. We have found that the use of a super duplex stainless steel modified carbon paste electrode significantly enhances the sensitivity to detect the oxidation of ascorbic acid. SAF-2507-grade stainless steel is used for the electrochemical biosensing of marine and medical applications. This material is selected in sensor applications since it has high corrosion resistance, stability in many aggressive environments, great biocompatibility, versatility, scalability, easy fabrication, and low cost compared to other materials. Table 1 depicts the use of various alloys used as a modifier to determine different bio-active molecules as reported.

Table 1. Studies reported by various researchers on cyclic voltammetry.

Elemental Composition	Electrochemical Technique	Chemical Constituent Used	Observations	Reference No.
Fe-18Cr-13Ni	Cyclic voltammetry	Dopamine, ascorbic acid, and uric acid	Since the 4 mg duplex modified carbon paste electrode exhibits a maximal anodic peak current of 25.61 µA, it is utilized as a modifier to examine the electrochemical characteristics of dopamine, ascorbic acid, and uric acid.	[39]
Fe-18Cr-13Ni	Cyclic voltammetry	Folic acid	The electrode process is controlled by electrode diffusion, and the anodic peak current rises linearly with correlation coefficient. The oxidation peak current is found to be 8.67 µA at 50 mV s^{-1} and 17.32 µA at 300 mV s^{-1}, respectively.	[40]
23Fe-21Cr-18Ni-20Ti-18Mn High Entropy Alloy	Cyclic voltammetry	Ascorbic Acid	For the concentration of 8 mg modifier, a maximum peak current of 104.07 µA was measured. For the high entropy alloy modified carbon paste electrode and the bare carbon paste electrode, the active surface areas for the electron transfer process of ascorbic acid are calculated to be 0.0014 cm^2 and 0.0027 cm^2, respectively.	[41]
Fe-18Cr-13Ni	Cyclic voltammetry	Dopamine, ascorbic acid, and uric acid	The 8 mg yttria dispersed duplex stainless steel modified carbon paste electrode has an anodic peak current of 31.01 µA, demonstrating significant electrocatalytic activity towards the oxidation of dopamine, ascorbic acid, and uric acid.	[42]
25Fe-19Cr-19Ni-18Ti-19Mn High Entropy Alloy	Cyclic voltammetry	Methylene Blue	The anodic peak current of 508.4 µA was displayed by the 4 mg high entropy alloy modified carbon paste electrode, while only 99.74 µA was displayed by the bare carbon paste electrode. This significant anodic peak current difference between the two different electrodes has demonstrated the value of the modifier in enhancing the electrode sensor's sensitivity, robustness, and selectivity.	[43]
2507 super duplex stainless steel	Cyclic voltammetry	Ascorbic acid	BCPE has shown an anodic peak current of 22.5 µA and 4 mg SDSS-MCPE has recorded 37.2 µA of anodic peak current during the electro-oxidation of 1 mM AA	Current Paper

2. Materials and Methods

2.1. Fabrication of SDSS Powders by Mechanical Alloying

The starting material used is SAF-2507 SDSS supplied by Sandvik Osprey Ltd, Neath, United Kingdom. The powder was ball milled in a Retsch PM-100, (Retsch GmbH, Haan, Germany) for 20 h at a ball-to-powder weight ratio of 10:1 and a mill speed of 250 rpm. The grinding medium consists of a 500 mL steel vial filled to about 40% of its capacity with 250 gm of stainless steel balls (Ø = 0.5 mm) and 25 gm of powder sample. Before beginning the experiment, the planetary ball mill jars and balls were cleaned by running the ball mill in a toluene atmosphere. The planetary ball mill is operated for 20 h by halting it for 30 min every two hours to prevent the jar from heating up too much.

The powder morphology was investigated using a Malvern Panalytical diffractometer, London, United Kingdom with Cu K-Alpha radiation (1.54060 Å) and a scanning electron microscope (TESCAN VEGA3 LMU) (RSAY HOLDING, Brno-Kohoutovice, Czech Republic) at an accelerating voltage ranging from 200 V to 30 Kv. Particle size analysis is carried out using the Anton Par-Zeta potential, (Anton Paar Germany GmbH, Ostfildern, Germania), and a particle size analyzer (3.1 Litesizer^{TM} 500, New South Wales, Australia). Figure 1 depicts the graphical representation of the experiment.

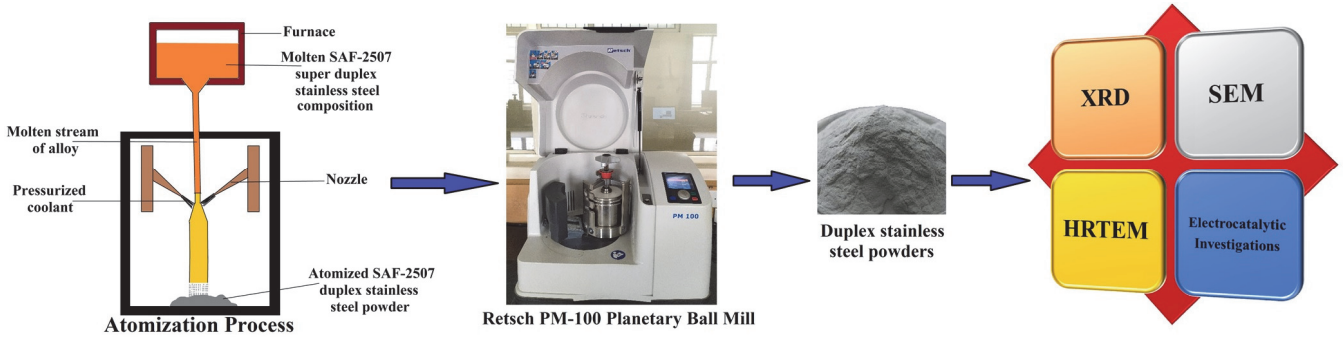


Figure 1. Graphical representation of the experiment.

2.2. Preparation of Carbon Paste Electrodes

The BCPE was prepared by hand grinding the graphite powder and silicone oil in a ratio of 70:30 in a mortar for 30 min [44]. On the other hand, the SDSS-MCPE were prepared by hand grinding the BCPE mixture along with various concentrations of SDSS powders (2, 4, 6, 8, and 10 mg) individually for 30 min each. The electrode system, the Zive SP1 galvanostat/potentiostat, (WonATech Co., Ltd., Seoul, Republic of Korea) was used to study the electrochemical sensor applications of the electrode. The details of the potentiostat are well discussed by the authors in their previous publications [45,46]. The working electrode has a 3 mm cavity connected to the copper wire, and the wire is connected to the potentiostat. The fabricated carbon paste electrodes were inserted into the cavity, which acts as a working electrode, and the current response was recorded during the electro-oxidation of ascorbic acid. All the chemicals, such as ascorbic acid, sodium hydrogen phosphate, and sodium dihydrogen phosphate, were purchased from Sigma-Aldrich, St. Louis, MO, United States.

3. Results

3.1. XRD Phase Analysis

Figure 2 shows the XRD spectra of the as-received and 20 h ball-milled SDSS powder. The as-received SDSS powder particles are spherical with an average particle size of 45 to 60 µm. After 20 h of ball milling, peak broadening was observed. This is due to the fracture of powder particles into flakes and subsequent reduction in grain size and amorphization. Mendonça et al., noted a similar phenomenon after 20 h of ball milling the duplex stainless steel UNS S31803 in a planetary mill [47]. The SAF-2507 super duplex stainless steel exhibits ferritic phase (α) up to 15 h of ball milling. The (110) peak shifts towards the lower angle

as the milling progresses, indicating the formation of austenite phase (111). Milling time promotes Cr and Ni atom diffusion into the Fe lattice, and these atoms vanish after each milling cycle [48–51]. The milling time was increased to reduce the intensity of the Fe peaks.

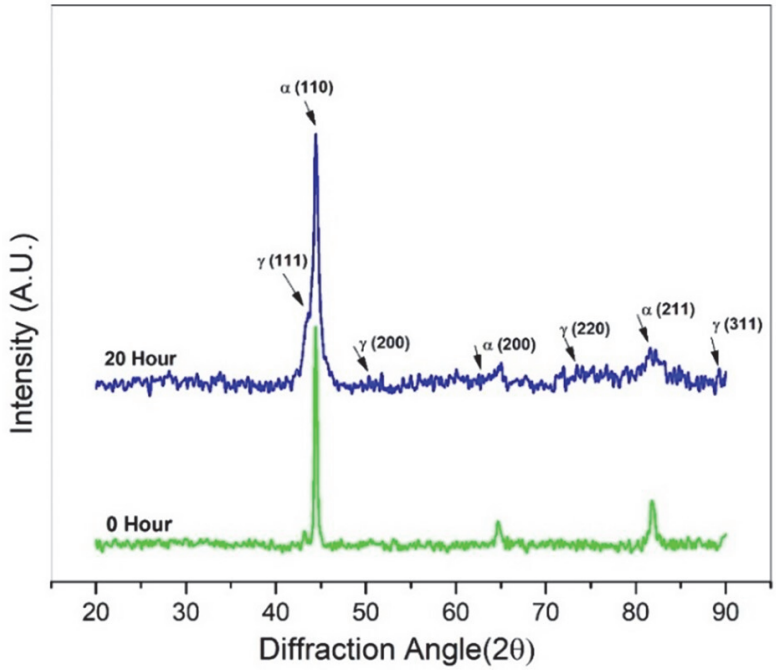


Figure 2. XRD Plots of as-received and 20 h ball-milled SAF-2507 SDSS Powder.

3.2. Powder Morphology Studies

Figure 3a depicts an SEM micrograph of an as-received powder sample with an average particle size of 45 to 60 µm, while Figure 3b depicts an SEM micrograph of a 20 h ball-milled SAF-2507 super duplex stainless steel powder. Figure 3c shows an EDS analysis of an SDSS powder sample to determine its elemental composition. The powder particles were discovered to be large and asymmetrical prior to milling. After five hours of ball milling, the particles begin to coalesce and flatten due to the ductility of Fe. However, after milling for up to 20 h, the ductile powder granules begin to refine, Ni and Cr become trapped in the Fe lattice, and the powder particles become work-hardened. Ni and Cr are evenly distributed throughout Fe to form an alloy. It has been discovered that 20 h of milling produces tiny, spherical powder granules of stainless steel [52]. The particle size of the 20 h milled DSS powder is approximately 5–7 µm, according to the micrographs, whereas the particle size of the powder as-received is approximately 30–45 µm. According to the literature, longer periods of ball milling increase contamination and the formation of intermetallic phases; thus, milling time is the most important parameter in mechanical alloying [53].

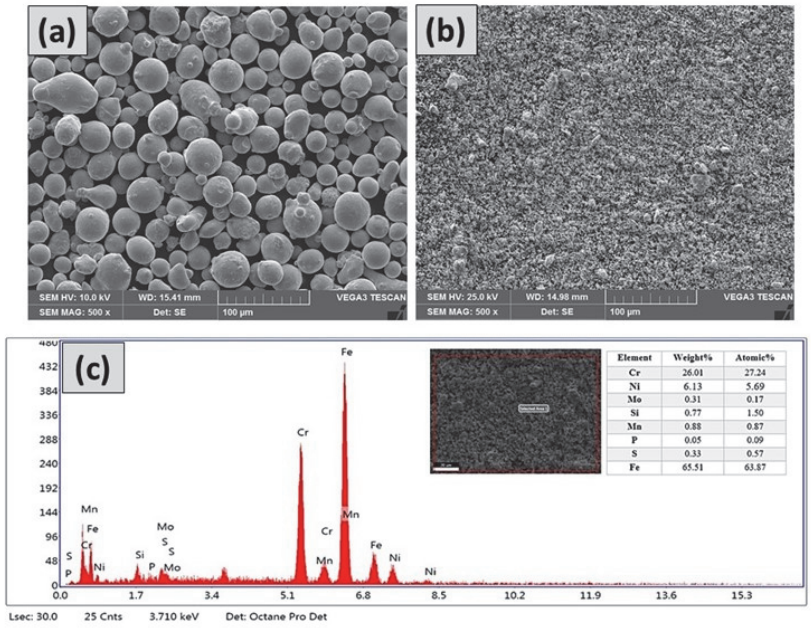


Figure 3. (**a**) SEM micrograph of as-received SAF-2507 SDSS powder, (**b**) SEM micrograph of 20 h ball-milled SAF-2507 SDSS powder, (**c**) EDS analysis.

3.3. Particle Size Analysis

The particle size plots of as-received and 20 h ball-milled SAF-2507 super duplex stainless steel powder are shown in Figure 4. Powder particles are nearly spherical in shape before ball milling, but due to severe plastic deformation, a phase transformation occurs, resulting in a two-phase alloy mixture containing nearly equal amounts of ferrite and austenite [54,55]. The particle size gradually decreases as the ball milling time increases. In the case of 20 h ball-milled powder, the size distribution curve will shift to the right, indicating grain refinement. Similar findings were made by Dharmalingam et al., who concluded that ball milling for 15–20 h increased peak broadening and significantly decreased crystallite size. [56]. The as-received powder had an average particle size of 536.8 nm, whereas the ball-milled sample had a particle size of around 200.9 nm after 20 h.

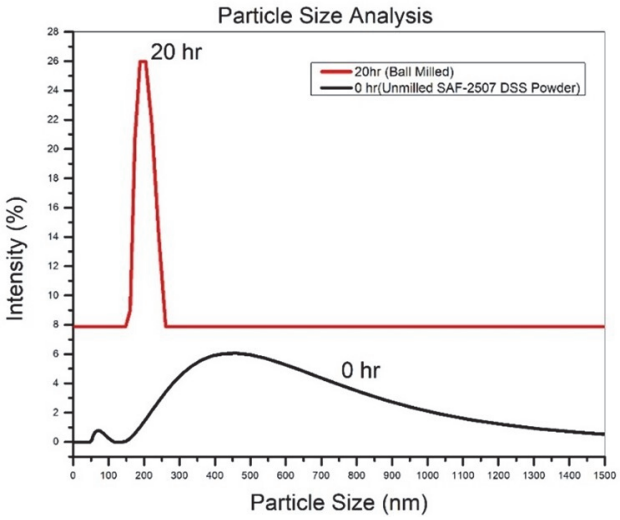


Figure 4. Particle size analysis of 20-h ball-milled SAF-2507 SDSS powder.

3.4. High-Resolution Transmission Electron Microscopy

Figure 5a,b show bright-field TEM images of SAF-2507 SDSS powder after ball milling for 20 h, and Figure 5c shows the SAED pattern. The black region in the bright

field TEM image represents microcrystal zones, while the whitish bright spots represent nanocrystals [57]. Rajendrachari et al., observed spherical crystals of austenitic stainless steels which are black in color with an average particle size of 10 to 20 nm. [11]. The lattice spacing of austenite (111) is shown in Figure 5b and is found to be 2.17 Å. The SAED pattern depicts the ferrite lattice spacing in Figure 5c. The TEM image shows fine agglomerated particles with sizes ranging from 10 to 50 nm. The studies show that the HRTEM and SEM micrographs show large particle size variations ranging from nanometers to micrometers.

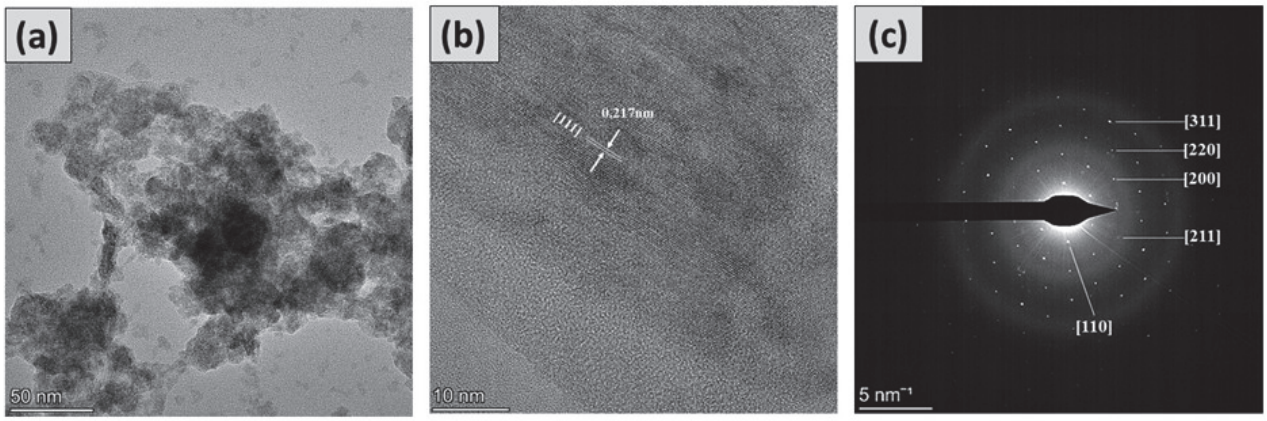


Figure 5. (**a**) HRTEM micrograph of as-received SAF-2507 SDSS powder, (**b**) HRTEM micrograph showing lattice spacing of [111] plane, (**c**) SAED Pattern of SAF-2507 SDSS powder.

3.5. Investigation of Electrochemical Sensor Applications

3.5.1. Electro-Oxidation of Ascorbic Acid at Different Concentrations of SDSS-MCPE

Generally, the concentration of the modifier used plays an important role in obtaining excellent current response during the determination of the analytes. Therefore, at the beginning of the experiment, we optimized the concentration of the SDSS-MCPE to record maximum current sensitivity during the electro-oxidation of AA in a phosphate buffer solution (PBS) with a pH of 6.8. We have used BCPE (0 mg), and 2, 4, 6, 8, and 10mg SDSS-MCPE to study the effect of modifier concentration to determine 1 mM AA, and their respective cyclic voltammograms are shown in Figure 6a. Figure 6b depicts the graph of anodic peak current (I_{Pa}) obtained with respect to the different modifier concentrations. From the graph, BCPE has shown the least current sensitivity of all the MCPEs. Among all, 4 mg SDSS-MCPE has shown almost two-fold more anodic peak current than the BCPE. This confirms the importance of the modifier which can determine the analytes even in low concentrations with significant current sensitivity. Figure 6c displays the cyclic voltammograms of BCPE and 4 mg SDSS-MCPE and it clearly shows the differences in their current responses. BCPE has shown an anodic peak current of 22.5 µA, and 4 mg SDSS-MCPE has recorded 37.2 µA of anodic peak current during the electro-oxidation of 1 mM AA. The increased I_{Pa} in the case of 4 mg SDSS-MCPE is due to the increase in the surface area and increased reaction sites.

To understand the effect of surface area on the I_{Pa}, we have calculated the electrode's active surface area by Randles–Sevcik equation [58–60], as depicted below,

$$i_p = 2.69 \times 10^5 n^{3/2} A D^{1/2} C \vartheta^{1/2} \quad (1)$$

The calculated active surface area of the BCPE and 4 mg SDSS-MCPE is found to be 0.0455 and 0.0754 cm^2, respectively. The increase in the surface area of the MCPE increases the reactive sites which in turn increases the interaction of electrons between the electrode and the analyte. As a result of which, 4 mg SDSS-MCPE has shown maximum current response during the electro-oxidation of 1 mM AA.

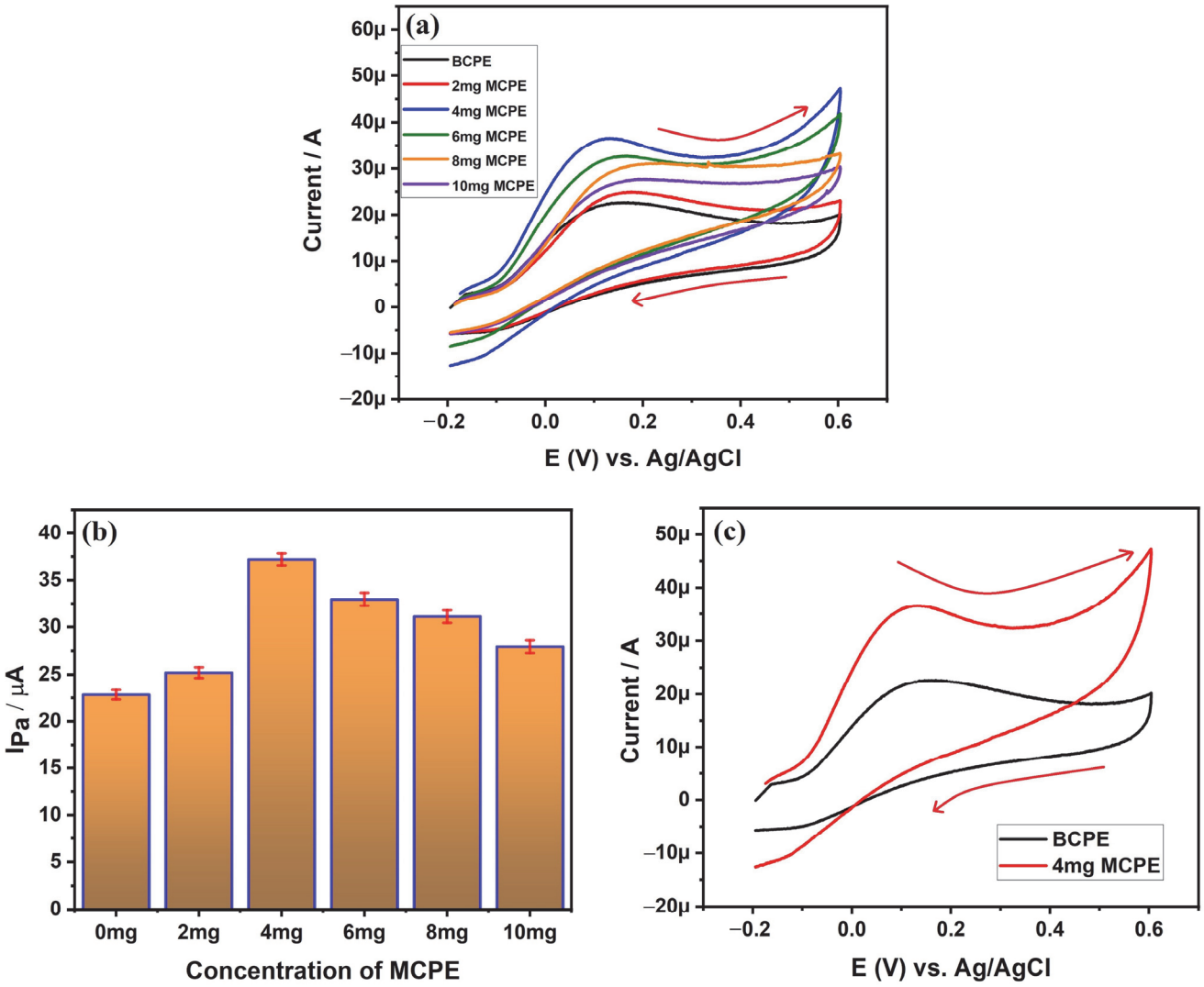


Figure 6. (**a**) Cyclic voltammogram of 1mM AA at different concentrations of the modifier. (**b**) Graph of different concentrations of the SDSS powders in MCPE and their respective I_{Pa}. (**c**) Voltammogram of 1 mM AA at BCPE and 4mg SDSS-MCPE.

3.5.2. Investigating the Influence of pH

Selecting a suitable pH is very important to understand the number of electrons and protons involved in the electrode reaction; also, a few analytes are stable in an acidic pH and a few more in a basic pH [61,62]. This in turn affects the stability of the analyte in a particular pH; therefore, we have investigated the effect of various pH conditions (acidic and basic range) on the electro-oxidation of AA.

Figure 7a depicts the voltammograms of electro-oxidation of 1 mM AA in various pH conditions ranging from 6 to 8. The highest I_{Pa} was recorded at a pH of 6.8, confirming the stability of the AA at that pH. Therefore, we have used a PBS with a pH of 6.8 for the rest of the electrochemical analysis. As we see from Figure 7a, the anodic peak potential is shifting towards the lower values; this confirms the participation of protons in the electrode reaction, whereas the I_{Pa} increases from pH 6 to 6.8 and then decreases. Figure 7b shows the graph of anodic peak potential vs. different pH measurements. From the graph, it is clearly seen that the increase in the pH of the electrolyte is shifting the peak potential towards the negative values. The graph of variation of the anodic peak potential with pH is linear and follows the equation, E_p (V) = 0.8960 − (0.061) pH (V/pH) (R2 = 0.9885), with an excellent linear regression coefficient (R2). This confirms the dependency of electron transfer during the oxidation and reduction of ascorbic acid on protonation. To understand

the electrode reaction in detail, we have calculated the number of electrons and protons involved using the below equation,

$$\frac{\Delta E_p}{\Delta pH} = \frac{2.303mRT}{nF} \quad (2)$$

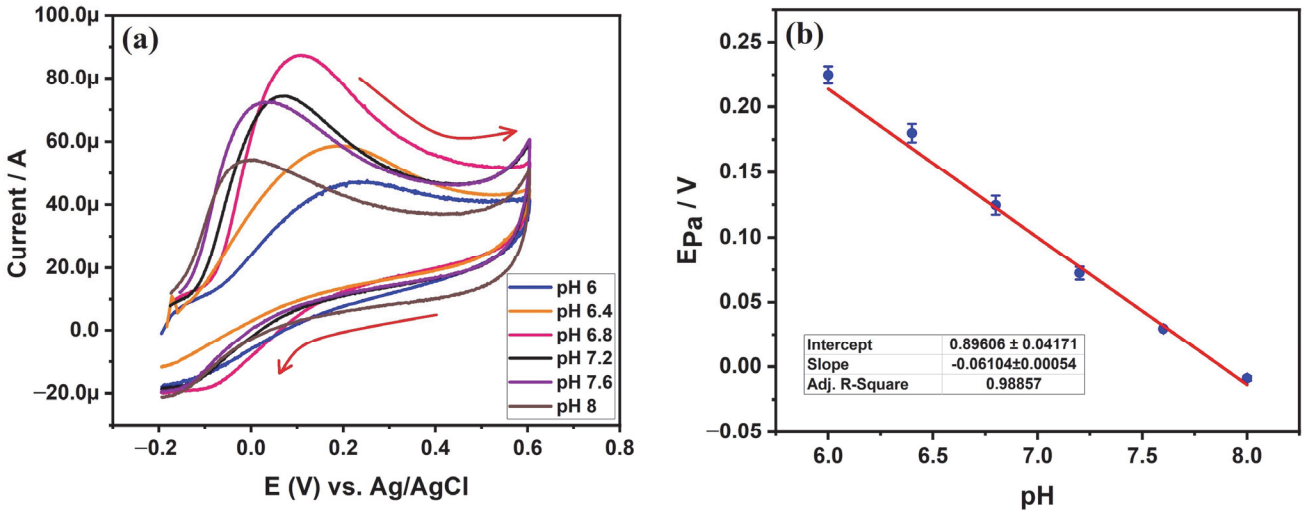


Figure 7. (**a**) Electrochemical oxidation of 1 mM AA at various pH PBS with a scan rate of 0.1 Vs^{-1}. (**b**) Graph of pH vs. E_{Pa} at 1 mM AA.

Where R is the gas constant, T is the temperature in kelvin, n is the number of electrons, and F is the Faraday constant. The number of protons (m) involved in the electro-oxidation of AA is calculated to be 2.064, and the value is almost equal to 2. Therefore, the electrochemical oxidation reaction of AA is taking place with the involvement of two electrons and two protons.

3.5.3. Influence of Scan Rate

To understand the type of electrochemical reaction and the stability of the fabricated MCPE, we have performed the electrochemical oxidation of 1 mM AA at different scan rates. This will confirm the type of electrochemical reaction, whether it is an absorption or diffusion-controlled reaction.

Therefore, we recorded the cyclic voltammetric response of 1 mM AA at different scan rates from 0.1 to 0.6 V/s, as shown in Figure 8a. The figure confirms the increase in the I_{Pa} with the increase in the scan rate from 0.1 to 0.6 V/s with a shifting of peak potential towards higher values. As we know, an increase in the scan rate decreases the time to keep the same charge value, and therefore, the current increases. Therefore, the increase in scan rate increases the anodic peak current value during the electro-oxidation of AA [63]. We plotted the graphs of scan rate versus I_{Pa} as depicted in Figure 8b. We can observe that the graph is linear and there is a gradual increase in the anodic peak current indicating the fast and direct electron transfer between AA and the surface of the 4 mg SDSS-MCPE. This linear increase in the anodic current against the scan rate also displays the strong binding character of AA molecules on the SDSS-MCPE. The correlation coefficient for Figure 8b was found to be 0.9968, and this confirms the electrode reaction is diffusion controlled.

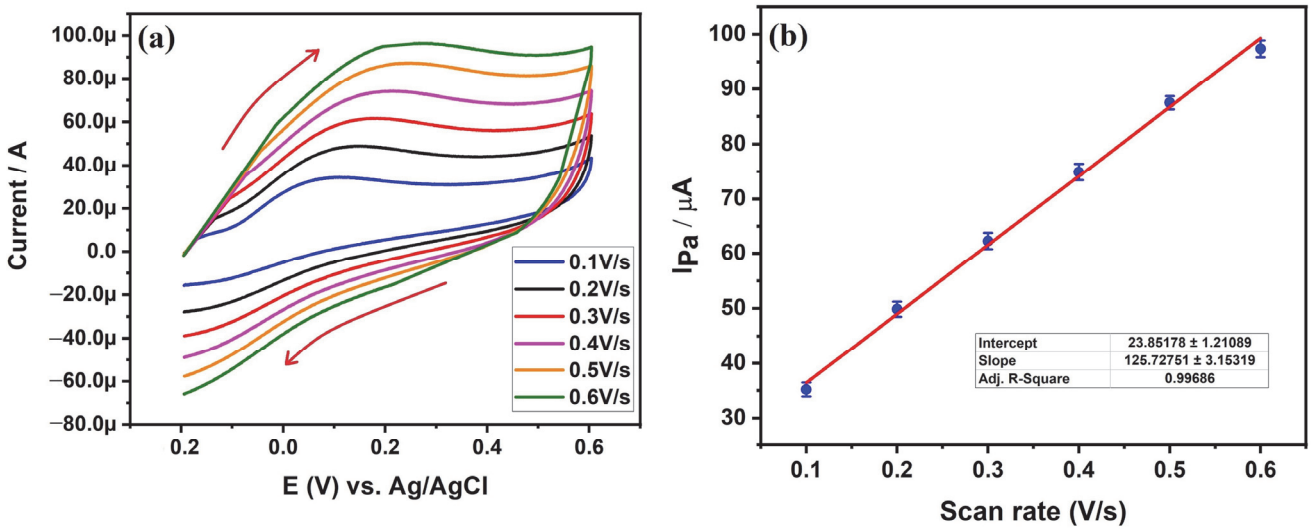


Figure 8. (**a**) Electrochemical oxidation of 1 mM AA at different scan rates ranging from 0.1 to 0.6 V/s. (**b**) The plot of I_{Pa} vs. scan rate at a pH of 6.8 PBS.

3.5.4. Influence of Concentration of AA

In general, as the concentration of the analyte is increased, then the peak current will also increase [64,65]. Therefore, the current response of all the analytes mainly depends upon their concentrations. Hence, we have studied the effect of concentrations of the AA on I_{Pa} during its electrochemical oxidation, and this will also help us to understand the stability and effectiveness of the fabricated SDSS-MCPE. Figure 9a depicts the cyclic voltammograms reported at different concentrations of the AA from 1 to 6 mM at a PBS pH of 6.8. The figure is confirming that an increase in the concentration of AA from 1 mM to 6 mM increased the I_{Pa} from 35 µA to 201 µA, respectively. We can also observe a linear increase in the I_{Pa} with the increase in the AA concentration, as shown in Figure 9b. This is due to the enhanced interaction of the AA molecules with SDSS-MCPE and the electrolyte; this increases the electron mobility and therefore increased anodic current. Hence, the highest I_{Pa} was obtained for the 6 mM AA concentration with a correlation coefficient of 0.9934.

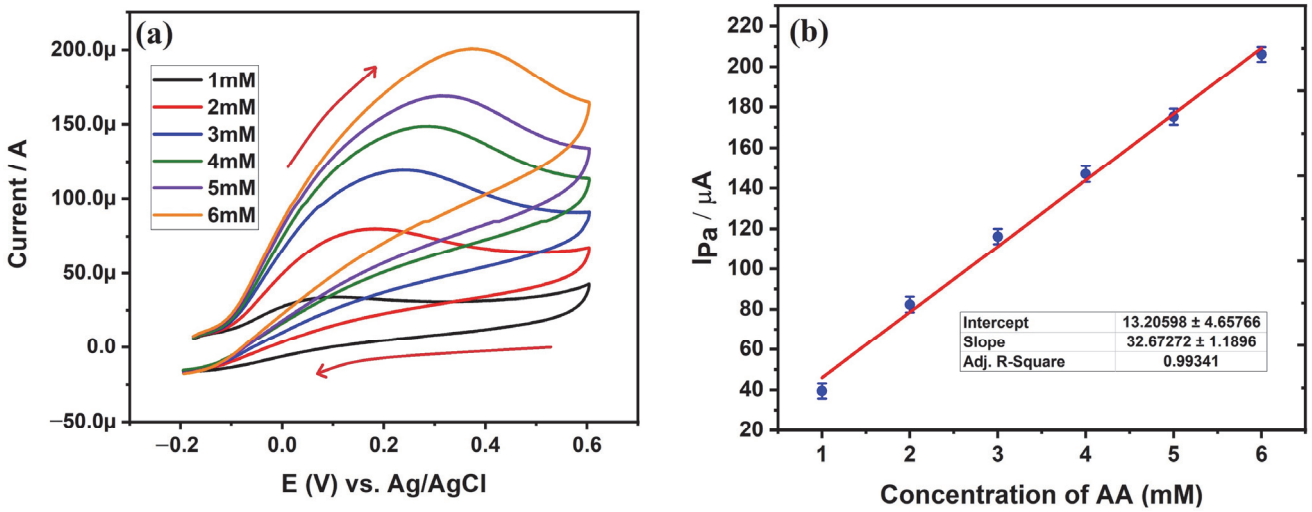


Figure 9. (**a**) Electrochemical oxidation of different concentrations of AA. (**b**) Plot of I_{Pa} versus the concentration of AA.

The possible mechanism of electro-oxidation of AA using 4mg SDSS-MCPE in a PBS of pH 6.8 is shown in Figure 10. The limit of detection (LD) and the limit of quantification (LQ)

of the 4 mg SDSS-MCPE were determined using the slope of Figure 9b and the standard deviation of the blank voltammogram (five cycles), respectively, using Equations (3) and (4), as follows,

$$\text{LD} = \frac{(3 \times \text{Standard deviation of Blank})}{\text{Slope of } I_{pa} \text{ versus concentration of AA}} \quad (3)$$

$$\text{LQ} = \frac{(10 \times \text{Standard deviation of Blank})}{\text{Slope of } I_{pa} \text{ versus concentration of AA}} \quad (4)$$

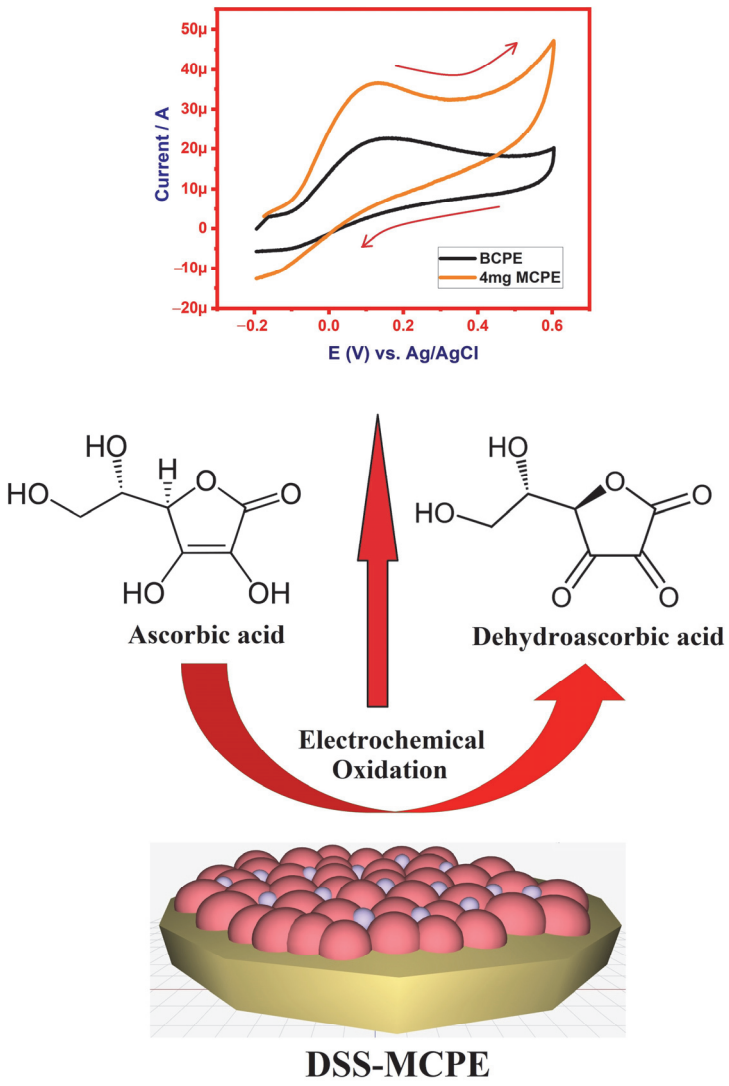


Figure 10. The possible electro-oxidation of AA using 4mg SDSS-MCPE in a PBS with a pH of 6.8.

The value of LD and LQ was calculated to be 0.206×10^{-8} M and 0.688×10^{-8} M, respectively, for the fabricated 4 mg SDSS-MCPE. The blank voltammogram (five cycles) used to calculate the standard deviation is shown in Figure 11.

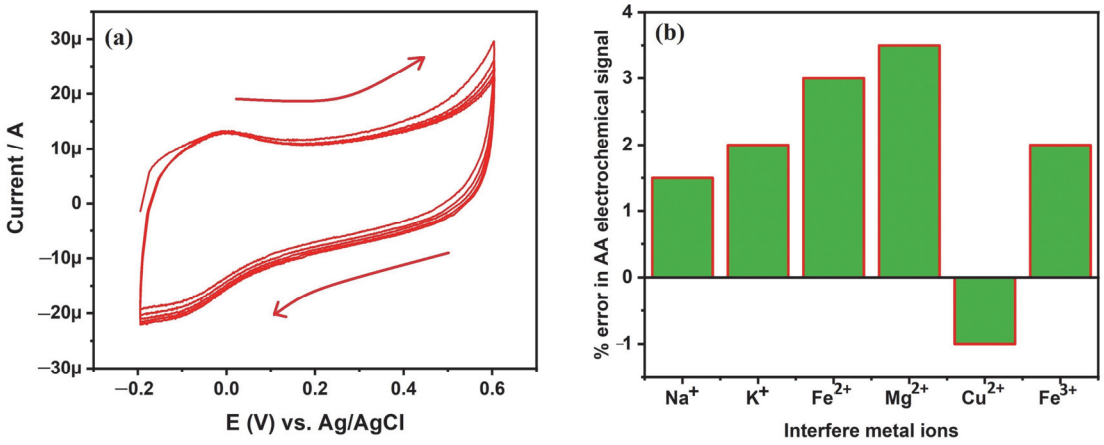


Figure 11. (**a**) The blank voltammogram (5 cycles) to calculate the standard deviation. (**b**) The plot of interfering metal ions versus % of error in the electrochemical signal of AA.

3.5.5. Interference Ions' Influence on AA during Its Electro-Oxidation at 4 mg SDSS-MCPE

The electrochemical oxidation of 1mM AA at 4 mg SDSS-MCPE was performed along with a few interfering metal ions to understand any significant variation in the current response or shifting of potential. In the present paper, we have used metal ions such as Na^+, K^+, Fe^{2+}, Mg^{2+}, Cu^{2+}, and Fe^{3+} to study their electrochemical interference with a 1 mM AA using SDSS-MCPE in a PBS with a pH of 6.8. From the experiment, we have observed that the electrochemical signal of AA was not influenced much in the presence of various metal ions as compared to the initial pure AA (without interfering metal ions) electrochemical signal. The variation in the electrochemical signal was reported to be less than ±4%, as shown in Figure 11. These results confirm that the fabricated 4 mg SDSS-MCPE electrode is highly selective and stable even in the presence of various interfering metal ions.

3.5.6. Repeatability, Reproducibility, and Stability of 4 mg SDSS-MCPE

The reproducibility, repeatability, and stability of the 4 mg SDSS-MCPE were investigated by electro-oxidizing the AA in a PBS with a pH of 6.8 with a scan rate of 0.1 V/s. The reproducibility and repeatability were performed five times each by changing the electrode and the electrolyte respectively. The calculated relative standard deviations of 3.02% and 2.15% were obtained for reproducibility and repeatability, respectively. These results suggest that the fabricated SDSS-MCPE is more repeatable and reproducible for the detection of AA molecules with almost no variation in the anodic peak current. We have also studied the stability of the fabricated SDSS-MCPE by running 50 cycles for the detection of AA in a pH 6.8 PBS. The extent of stability is calculated by recording the initial and the final anodic peak current during the electro-oxidation of AA. The stability value was calculated to be 96.98%; this confirms that the fabricated SDSS-MCPE has depicted excellent stability during the electrochemical detection of AA in a PBS with a pH of 6.8.

4. Conclusions

Mechanical alloying for up to 20 h is required to produce nanostructured SAF-2507 super duplex stainless steels. The milling time is the most important parameter for achieving a steady state between powder particle fracturing and cold welding. After 15 h of planetary ball milling, XRD results revealed a phase transition from ferrite (α) to austenite (γ). The phase transformation is caused by severe plastic deformation. After 20 h of ball milling, the average particle size was about 200.9 nm. HRTEM analysis revealed fine agglomerated particles with sizes ranging from 10 to 50 nm. The experiment revealed that the electrochemical signal of ascorbic acid was not significantly altered by the presence of various metal ions as compared to the original pure ascorbic acid. We investigated the influence of ascorbic acid concentrations on I_{Pa} during electrochemical oxidation, which will help us understand the stability and effectiveness of the fabricated SDSS-MCPE.

Author Contributions: Conceptualization, methodology, writing—original draft preparation, R.S.M.; funding acquisition, resources, S.V.; review and editing, conducting a research and investigation process, specifically performing the experiments, S.R.; data curation, visualization, and provision of study materials, S.P.C.; data curation, visualization, D.N.; Writing—review and editing, resources, N.B. All authors have read and agreed to the published version of the manuscript.

Funding: This research was supported by the Ministry of Science and Technology, Department of Science and Technology, Seed Division, New Delhi, India (Grant No. SP/YO/2019/948) which is gratefully acknowledged.

Data Availability Statement: Data available on request due to restrictions e.g. privacy or ethical. The data presented in this study are available on request from the corresponding author. The data are not publicly available due to the privacy.

Acknowledgments: The authors acknowledge the support from REVA University, Bengaluru, India to carry out the research work.

Conflicts of Interest: The authors declare no conflict of interest.

References

1. Philip Selvaraj, D.; Chandramohan, P.; Mohanraj, M. Optimization of surface roughness, cutting force and tool wear of nitrogen alloyed duplex stainless steel in a dry turning process using Taguchi method. *Measurement* **2014**, *49*, 205–215. [CrossRef]
2. Jan, O.; Malin, S. Duplex—A new generation of stainless steels for desalination plants. *Desalination* **2007**, *25*, 104–113.
3. Wang, Y.Q.; Yang, B.; Han, J.; Dong, F.; Wang, Y.L. Localized corrosion of thermally aged cast duplex stainless steel for primary coolant pipes of nuclear power plant. *Procedia Eng.* **2012**, *36*, 88–95. [CrossRef]
4. Schofield, M.J.; Bradsha, R.; Cottis, R.A. Stress Corrosion cracking of duplex stainless-steel weldments in sour conditions. *Mater. Perform.* **1996**, *36*, 65–70.
5. Shashanka, R.; Chaira, D. Effects of Nano-Y_2O_3 and Sintering Parameters on the Fabrication of PM Duplex and Ferritic Stainless Steels. *Acta Metall. Sin. (Engl. Lett.)* **2016**, *29*, 58–71. [CrossRef]
6. Tuba, K.; Hayriye, E.E.; Mustafa, T.; Ramazan, K. Strengthening of AISI 2205 duplex stainless steel by strain ageing. *Mater. Des.* **2014**, *55*, 250–256. [CrossRef]
7. Herenu, S.; Alvarez, A.; Armas, A.F. The influence of dynamic strain aging on the low cycle fatigue of duplex stainless steel. *Scr. Mater.* **2001**, *45*, 739–745. [CrossRef]
8. Hiroyuki, M.; Takuro, M.; Satoshi, H. Superplastic deformation of micro-specimens of duplex stainless steel. *Mater. Sci. Eng. A* **2001**, *319–321*, 779–783. [CrossRef]
9. Solomon, H.D.; Devine, T.M. *Duplex Stainless Steels*; American Society of Metals: Metals Park, OH, USA, 1983; pp. 693–756.
10. Marina, K.; Michael, P. Duplex Steels: Part I: Genesis, Formation, Structure. *Metallogr. Microstruct. Anal.* **2013**, *2*, 113–121. [CrossRef]
11. Shashanka, R.; Chaira, D. Development of nano-structured duplex and ferritic stainless steels by pulverisette planetary milling followed by pressureless sintering. *Mater. Charact.* **2015**, *99*, 220–229. [CrossRef]
12. Shashanka, R.; Chaira, D.; Dibyendu, C. Fabrication of Nano-Yttria Dispersed Duplex and Ferritic Stainless Steels by Planetary Milling Followed by Spark Plasma Sintering and Non-Lubricated Sliding Wear Behaviour Study. *J. Mater. Sci. Eng. B* **2016**, *6*, 111–125. [CrossRef]
13. Vannevik, H.; Nilsson, J.O.; Frodigh, J.; Kangas, P. Effect of Elemental Partitioning on Pitting Resistance of High Nitrogen Duplex Stainless Steels. *ISIJ Int.* **1996**, *36*, 807–812. [CrossRef]
14. Wang, J.; Uggowitzer, P.J.; Magdowski, R.; Speidel, M.O. Nickel-Free Duplex Stainless Steels. *Scr. Mater.* **1998**, *40*, 123–129. [CrossRef]
15. Kurzydlowski, K.J. Microstructural refinement and properties of metals processed by severe plastic deformation. *Bull. Pol. Acad. Sci.* **2004**, *52*, 301–311.
16. Shashanka, R. Non-lubricated dry sliding wear behavior of spark plasma sintered nano-structured stainless steel. *J. Mater. Environ. Sci.* **2019**, *10*, 767–777.
17. Williamson, G.K.; Hall, W.H. X-ray line broadening from filed aluminium and wolfram. *Acta Metall.* **1953**, *1*, 22–31. [CrossRef]
18. Oleszak, D.; Grabias, A.; Pekala, M.; Swiderska-Sroda, A.; Kulik, T. Evolution of structure in austenitic steel powders during ball milling and subsequent sintering. *J. Alloys Compd.* **2007**, *434–435*, 340–343. [CrossRef]
19. Rayappa, S.M.; Shashanka, R.; Shamanth, V.; Hemanth, K.; Nithin, S.K.; Sharath, P.C.; Adarsh, P. Technology and Challenges in Additive Manufacturing of Duplex Stainless Steels. *Biointerface Res. Appl. Chem.* **2022**, *12*, 1110–1119. [CrossRef]
20. Rayappa, S.M.; Shamanth, V.; Sharath, P.C.; Shashanka, R.; Hemanth, K. A Review on Spark Plasma Sintering of Duplex Stainless Steels. *Mater. Today Proc.* **2021**, *45*, 138–144. [CrossRef]
21. Rayappa, S.M.; Shamanth, V.; Hemanth, K.; Sharath, P.C.; Shashanka, R. Mechanical Testing of Spark Plasma Sintered Materials: A Review. *AIP Conf. Proc.* **2022**, *2469*, 020026. [CrossRef]

22. Ravnsbaek, D.B.; Sorensen, L.H.; Filinchuk, Y.; Besenbacher, F.; Jensen, T.R. Screening of metal borohydrides by mechanochemistry and diffraction. *Angew. Chem.* **2012**, *51*, 3582–3586. [CrossRef]
23. Morten, B.L.; Dorthe, B.R.; Yaroslav, F.; Lee, Y.-S.; Raphael, J.; Young, W.C.; Jorgen, S.; Torben, R.J. LiCe$(BH_4)_3$Cl a new lithium-ion conductor and hydrogen storage material with isolated tetranuclear anionic clusters. *Chem. Mater.* **2012**, *24*, 1654–1663. [CrossRef]
24. Huot, J.; Ravnsbaek, D.B.; Zhang, J.; Cuevas, F.; Latroche, M.; Jensen, T.R. Mechanochemical synthesis of hydrogen storage materials. *Prog. Mater. Sci.* **2013**, *58*, 30–75. [CrossRef]
25. Ravnsbaek, D.B.; Nickels, E.A.; Cerny, R.; Olesen, C.H.; David, W.I.F.; Edwards, P.P.; Filinchuk, Y.; Jensen, T.R. Novel Alkali Earth Borohydride $Sr(BH_4)_2$ and Borohydride-Chloride $Sr(BH_4)Cl$. *Inorg. Chem.* **2013**, *52*, 10877–10885. [CrossRef]
26. Radovan, C.; Pascal, S.; Yolanda, S.; Katarina, S.; Lubomir, S.; Ritcher, B.; Torben, R.J. Trimetallic borohydride $Li_3MZn_5(BH_4)_{15}$ (M=Mg, Mn) containing two weakly interconnected frameworks. *Inorg. Chem.* **2013**, *52*, 9941–9947. [CrossRef]
27. Meyers, M.A.; Mishra, A.; Benson, D.J. Mechanical properties of nanocrystalline materials. *Prog. Mater. Sci.* **2006**, *51*, 427–556. [CrossRef]
28. Shashanka, R.; Chaira, D. Phase transformation and microstructure study of nano-structured austenitic and ferritic stainless-steel powders prepared by planetary milling. *Powder Technol.* **2014**, *259*, 125–136. [CrossRef]
29. Haghir, T.; Abbasi, M.H.; Golozar, M.A.; Panjepour, M. Investigation of α to γ transformation in the production of a nanostructured high-nitrogen austenitic stainless-steel powder via mechanical alloying. *Mater. Sci. Eng. A* **2009**, *507*, 144–148. [CrossRef]
30. Amini, R.; Salahinejad, E.; Hadianfard, M.J.; Marasi, M.; Sritharan, T. Characterization of Fe–Cr–Mn–N amorphous powders with a wide supercooled liquid region developed by mechanical alloying. *Mater. Sci. Eng. A* **2010**, *527*, 1135–1142. [CrossRef]
31. Chen, M.; Liu, H.; Wang, L.; Xu, Z.; Ji, V.; Jiang, C. Residual stress and microstructure evolutions of SAF 2507 duplex stainless steel after shot peening. *Appl. Surf. Sci.* **2018**, *459*, 155–163. [CrossRef]
32. Li, J.; Ma, Z.; Xiao, X.; Zhao, J.; Jiang, L. On the behavior of nitrogen in a low-Ni high-Mn super duplex stainless steel. *Mater. Des.* **2011**, *32*, 2199–2205. [CrossRef]
33. Ayoub, H.; Lair, V.; Griveau, S.; Brunswick, P.; Bedioui, F.; Cassir, M. Electrochemical Characterization of Stainless Steel as a New Electrode Material in a Medical Device for the Diagnosis of Sudomotor Dysfunction. *Electroanalysis* **2012**, *24*, 1324–1333. [CrossRef]
34. Kitte, S.A.; Gao, W.; Zholudov, Y.T.; Qi, L.; Nsabimana, A.; Liu, Z.; Xu, G. Stainless steel electrode for sensitive luminol electrochemiluminescence detection of H2O2, glucose, and glucose oxidase activity. *Anal. Chem.* **2017**, *89*, 9864–9869. [CrossRef] [PubMed]
35. Bimakr, F.; Ginige, M.P.; Kaksonen, A.H.; Sutton, D.C.; Puzon, G.J.; Cheng, K.Y. Assessing graphite and stainless-steel for electrochemical sensing of biofilm growth in chlorinated drinking water systems. *Sens. Actuators B Chem.* **2018**, *277*, 526–534. [CrossRef]
36. Faria, R.A.D.; Luiz, G.; Dias, H.; Luiz, G.D.H.; Vanessa de, F.C.L. AISI 304 Stainless Steel as a Transducer Substrate in Electrochemical Biosensors for Medical Applications. *Biomed. J. Sci. Tech. Res.* **2019**, *18*, 13382–13388. [CrossRef]
37. Martínez-Ibernón, A.; Lliso-Ferrando, J.; Gandía-Romero, J.M.; Soto, J. Stainless Steel Voltammetric Sensor to Monitor Variations in Oxygen and Humidity Availability in Reinforcement Concrete Structures. *Sensors* **2021**, *21*, 2851. [CrossRef]
38. González, E.N.A.; Puente, D.S.L.; Muñiz, F.M.C.; Flores, S.E.; Martínez-Luévanos, A. Electrochemical Fabrication of a GO-NiO/AISI 316L Electrode and Its Evaluation for Glucose Detection. *Int. J. Electrochem. Sci.* **2021**, *16*, 21066. [CrossRef]
39. Shashanka, R.; Chaira, D.; Kumara Swamy, B.E. Electrochemical investigation of duplex stainless steel at carbon paste electrode and its application to the detection of dopamine, ascorbic and uric acid. *Int. J. Sci. Eng. Res.* **2015**, *6*, 1863–1871.
40. Shashanka, R.; Chaira, D.; Kumara Swamy, B.E. Electrocatalytic Response of Duplex and Yittria Dispersed Duplex Stainless Steel Modified Carbon Paste Electrode in Detecting Folic Acid Using Cyclic Voltammetry. *Int. J. Electrochem. Sci.* **2015**, *10*, 5586–5598. [CrossRef]
41. Liu, H.; Syama, L.; Zhang, L.; Lee, C.; Liu, C.; Dai, Z.; Yan, Q. High-entropy alloys and compounds for electrocatalytic energy conversion applications. *SusMat* **2021**, *1*, 482–505. [CrossRef]
42. Shashanka, R.; Chaira, D.; Kumara Swamy, B.E. Fabrication of yttria dispersed duplex stainless steel electrode to determine dopamine, ascorbic and uric acid electrochemically by using cyclic voltammetry. *Int. J. Sci. Eng. Res.* **2016**, *7*, 1275–1285.
43. Rajendrachari, S.; Adimule, V.M.; Jayaprakash, G.K.; Pandith, A. Electrochemical oxidation of methylene blue dye in wastewater using mechanically alloyed high entropy alloy modified carbon paste electrode using cyclic voltammetry. *Mater. Res. Express* **2023**, *10*, 054003. [CrossRef]
44. Rajendrachari, S.; Kudur Jayaprakash, G.; Pandith, A.; Karaoglanli, A.C.; Uzun, O. Electrocatalytic Investigation by Improving the Charge Kinetics between Carbon Electrodes and Dopamine Using Bio-Synthesized CuO Nanoparticles. *Catalysts* **2022**, *12*, 994. [CrossRef]
45. Shashanka, R.; Jayaprakash, G.K.; Prakashaiah, B.G.; Kumar, M.; Swamy, B.K. Electrocatalytic determination of Ascorbic Acid using a Green Synthesised Magnetite Nano-Flake Modified Carbon Paste Electrode by Cyclic Voltammetric method. *Mater. Res. Innov.* **2021**, *26*, 229–239. [CrossRef]
46. Jayaprakash, G.K.; Swamy, B.K.; Rajendrachari, S.; Sharma, S.C.; Roberto, F.-M. Dual Descriptor Analysis of Cetylpyridinium modified Carbon Paste Electrodes for Ascorbic Acid sensing Applications. *J. Mol. Liq.* **2021**, *334*, 116348. [CrossRef]

47. Mendonça, C.D.S.P.; Oliveira, A.F.; Oliveira, L.A.; da Silva, M.R.; Melo, M.D.L.N.M.; Silva, G. Structural and Magnetic Properties of Duplex Stainless steel (UNS S31803) Powders Obtained by high Energy Milling of Chips with Additions of NbC. *Mater. Res.* **2018**, *21*, e20170717. [CrossRef]
48. Torres, C.; Johnsen, R.; Iannuzzi, M. Crevice corrosion of solution annealed 25Cr duplex stainless steels: Effect of Won critical temperatures. *Corros. Sci.* **2020**, *178*, 109053. [CrossRef]
49. Li, J.; Zhang, Z.; Chen, H.; Xiao, X.; Zhao, J.; Jiang, L. New Economical 19Cr Duplex Stainless Steels. *Met. Mater. Trans. A* **2011**, *43*, 428–436. [CrossRef]
50. Llorca-Isern, N.; López-Luque, H.; López-Jiménez, I.; Biezma, M.V. Identification of sigma and chi phases in duplex stainless steels. *Mater. Charact.* **2016**, *112*, 20–29. [CrossRef]
51. He, L.; Wu, X.; Zhang, Z.; Li, J. Microstructure Evolution and Corrosion Behavior of Duplex Stainless Steel During Isothermal Aged at 650 °C. *Int. J. Electrochem. Sci.* **2016**, *11*, 8046–8056. [CrossRef]
52. Li, Z.; Wei, F.; La, P.; Wang, H.; Wei, Y. Enhancing Ductility of 1045 Nanoeutectic Steel Prepared by Aluminothermic Reaction through Annealing at 873K. *Adv. Mater. Sci. Eng.* **2017**, *2017*, 5392073. [CrossRef]
53. Mao, Y.; Zheng, Y.; Shi, Y.; Zhu, M.; Saitejin; Liu, S.; Lin, X.; La, P. Effect of rolling deformation on microstructure and mechanical properties of 2205 duplex stainless steel with micro-nano structure. *Mod. Phys. Lett. B* **2020**, *34*, 2050269. [CrossRef]
54. Nayak, A.K.; Shashanka, R.; Chaira, D. Effect of Nanosize Yittria and Tungsten Addition to Duplex Stainless Steel During High Energy Planetary Milling. *IOP Conf. Ser. Mater. Sci. Eng.* **2016**, *115*, 012008. [CrossRef]
55. Shashanka, R. Synthesis of nano-structured stainless-steel powder by mechanical alloying-an overview. *Int. J. Sci. Eng. Res.* **2017**, *8*, 588–594.
56. Dharmalingam, G.; Prasad, M.A.; Salunkhe, S. Optimization of milling speed and time in mechanical alloying of ferritic ODS steel through taguchi technique. *Int. J. Simul. Multidisci. Des. Optim.* **2021**, *12*, 25. [CrossRef]
57. Gupta, S.; Shashanka, R.; Chaira, D. Synthesis of nano-structured duplex and ferritic stainless-steel powders by planetary milling: An experimental and simulation study. *IOP Conf. Ser. Mater. Sci. Eng.* **2014**, *75*, 012033. [CrossRef]
58. Rajendrachari, S.; Basavegowda, N.; Vinaykumar, R.; Narsimhachary, D.; Somu, P.; Lee, M.-J. Electrocatalytic determination of methyl orange dye using mechanically alloyed novel metallic glass modified carbon paste electrode by cyclic voltammetry. *Inorg. Chem. Commun.* **2023**, *155*, 111010. [CrossRef]
59. Reddy, S.; Kumara Swamy, B.E.; Aruna, S.; Mohan, K.; Shashanka, R.; Jayadevappa, H. Preparation of NiO/ZnO hybrid nanoparticles for electrochemical sensing of dopamine and uric acid. *Chem. Sens.* **2012**, *2*, 7.
60. Rajendrachari, S.; Adimule, V.; Gulen, M.; Khosravi, F.; Somashekharappa, K.K. Synthesis and Characterization of High Entropy Alloy 23Fe-21Cr-18Ni-20Ti-18Mn for Electrochemical Sensor Applications. *Materials* **2022**, *15*, 7591. [CrossRef]
61. Manjunatha, J.G.; Deraman, M.; Basri, N.H.; Talib, I.A. Fabrication of poly (Solid Red A) modified carbon nano tube paste electrode and its application for simultaneous determination of epinephrine, uric acid and ascorbic acid. *Arab. J. Chem.* **2018**, *11*, 149–158. [CrossRef]
62. Hareesha, N.; Manjunatha, J.G.; Raril, C.; Tighezza, A.M.; Albaqami, M.D.; Mika, S. Electrochemically polymerized glutamine-activated graphite paste surface as a green biosensor for sensitive catechol detection in water samples. *J. Mater. Sci. Mater. Electron.* **2023**, *34*, 533. [CrossRef]
63. Alemu, T.; Zelalem, B.; Amare, N. Voltammetric Determination of Ascorbic Acid Content in Cabbage Using Anthraquinone Modified Carbon Paste Electrode. *J. Chem.* **2022**, *2022*, 7154170. [CrossRef]
64. Rajendrachari, S.; Nagaraj, B.; Adimule, V.M.; Baris, A.; Prathap, S.; Saravana Kumar, R.M.; Kwang-Hyun, B. Assessing the Food Quality Using Carbon Nanomaterial Based Electrodes by Voltammetric Techniques. *Biosensors* **2022**, *12*, 1173. [CrossRef] [PubMed]
65. Abd-Elsabour, M.; Keriman, M.; Abd-Elsabur, F.H.; Hasan, A.; Ibrahem, M.A. An Electrochemical Sensor Based on Poly(methyl orange) Modified Glassy Carbon Electrode for Simultaneous Determination of Vitamins B2 and C in Aqueous Solution. *Anal. Bioanal. Chem. Res.* **2022**, *9*, 259–268.

Disclaimer/Publisher's Note: The statements, opinions and data contained in all publications are solely those of the individual author(s) and contributor(s) and not of MDPI and/or the editor(s). MDPI and/or the editor(s) disclaim responsibility for any injury to people or property resulting from any ideas, methods, instructions or products referred to in the content.